



Special Feature: Energy Conversion and Storage

Review

Fabrication of $\text{Cu}_2\text{ZnSnS}_4$ Thin Film Solar Cells by Sulfurization

Tatsuo Fukano, Hiroshi Nozaki, Shin Tajima, Tadayoshi Ito, Akihiro Nagoya and Ryoji Asahi

Report received on Jul. 8, 2013

■ ABSTRACT ■ Several researches and developments on $\text{Cu}_2\text{ZnSnS}_4$ (CZTS) thin films and CZTS solar cells, which we have had intimate involvements in, are introduced. Based on the crystallographic study of CZTS thin films conducted by theoretical studies using first-principle calculations and analytical studies using synchrotron radiation X-ray diffraction, we proposed that they show uniform fundamental properties. The theoretical studies showed that the substitution of Cu at the Zn sites is the most stable defect and are the dominant acceptor sites in CZTS. The experimental researches showed that the CZTS thin films constituting high-performing solar cells possess the kesterite crystal structure with Zn at the $2d$ site substituted by Cu and/or with Cu at the $2c$ site substituted by Zn. Additionally, during the fabrication of CZTS thin films by sulfurization, they were found to be necessarily formed through the reaction $\text{Cu}_2\text{SnS}_3 + \text{ZnS} \rightarrow \text{Cu}_2\text{ZnSnS}_4$. We succeeded in improving the conversion efficiency of CZTS thin film solar cells by investigating and refining the sulfurization conditions. We attribute the lower efficiencies of CZTS solar cells compared to that of $\text{Cu}(\text{In,Ga})\text{Se}_2$ (CIGS) solar cells to the enormous number of recombination centers between the CZTS absorber and CdS buffer layers.

■ KEYWORDS ■ Solar Cell, Photovoltaics, $\text{Cu}_2\text{ZnSnS}_4$, Kesterite, Compound Semiconductor, Thin Film, Sulfurization, Heterojunction, First-principle Calculation, X-ray Anomalous Dispersion

1. Introduction

At present, solar cells are attracting considerable interest as the next-generation renewable energy sources to replace conventional fossil-fuel-based energy sources. Approximately 90% of the solar cells are currently made from Si because of its abundance on the earth's crust, lack of toxicity, chemical stability, and established processing technologies. However, there are some practical limitations to reducing the production cost of solar cells, which include the use of high-cost processes such as purification (to obtain ultra-high purity Si) and bulk crystallization. In contrast to Si solar cells, thin film solar cells based on other compounds such as CdTe can reduce the production cost without the need for ultra-high purity raw materials and bulk crystallization. However, CdTe thin film solar cells, which are known for their low production cost, consist of toxic materials such as Cd and Te. Further, $\text{Cu}(\text{In,Ga})(\text{S,Se})_2$ (CIGS) thin film solar cells exhibit approximately the same module conversion efficiency as polycrystalline Si solar cells. It is noteworthy that the production cost of CIGS solar cells is lower than that of polycrystalline Si solar cells. Therefore, the production volume of CIGS solar cells

has rapidly increased. However, because In and Ga are rare metals as well as strategic materials, their market prices undergo many changes. It is possible that the production cost of CIGS cells will hereafter increase due to the increasing prices of rare metals with increase in production volume. Thus, in order to bring down the production cost, we need to develop solar cells based on new materials, and solar cells based on $\text{Cu}_2\text{ZnSnS}_4$ (CZTS) are strong contenders.

CZTS and $\text{Cu}_2\text{ZnSn}(\text{S}_x\text{Se}_{1-x})$ (CZTSSe) have been explored for use as p -type semiconductor absorber layers in thin film solar cells. In particular, CZTS possesses a suitable optical bandgap of 1.4–1.5 eV.^(1,2) Its photovoltaic properties were confirmed by Ito et al. in 1988.⁽³⁾ Katagiri et al.⁽⁴⁾ and Friedlmeier et al.⁽⁵⁾ independently reported CZTS solar cells in 1996 and 1997, respectively. Further, after fabricating CZTS solar cells with conversion efficiency exceeding 6% in 2008,⁽⁶⁾ the efficiencies of CZTS and CZTSSe solar cells have been rapidly improved.^(7–12) The developments in the conversion efficiencies of CZTS and CZTSSe solar cells are shown in **Table 1**.^(2–10,12,13–19) Our research has focused on CZTS thin film solar cells, which contain no toxic materials such as Se.

This review discusses our research studies on CZTS

solar cells. Because the crystal structure strongly affects the ability of a material to produce electric power, it is very important to understand the relationship between the composition and the crystal structure of CZTS thin films. Hence, first, the theoretical studies of the crystal structure of CZTS and the experimental studies of the crystal structure of CZTS thin films are described. Next, the formation of CZTS thin films and the various properties of CZTS solar cells are described, specifically in the context of the conversion efficiencies of CZTS solar cells.

2. Preparation of Solar Cells

The CZTS thin films were prepared by sulfurization carried out by heating the thin film precursors in H₂S gas or S vapor. Sulfurization produces crystalline films and homogeneous compositions, and is suitable for the production of commercial CIGS solar cells because of the low production cost and good productivity of large-area solar cells.

The method used for preparing CZTS solar cells possessing the device structure shown in **Fig. 1** is described below. The cell structure does not include a high resistance buffer layer and an antireflection

coating. **Figure 2** illustrates the method of preparation. First, 1- μ m-thick Mo electrode layers were fabricated on alkali glass substrates by sputter deposition. Approximately 1000-nm-thick CZTS precursors were deposited by RF (radio frequency) magnetron sputtering using either pure metal or metal sulfide targets. CZTS absorber layers were obtained by sulfurizing the CZTS precursors. The sulfurization was carried out by heating the precursors to 560–580 °C and by maintaining the precursors at this temperature for a given holding time in an atmosphere of 20 vol% H₂S balanced with N₂. The heating and cooling rates varied from 5 to 10 °C/min and from –5 to –10 °C/min, respectively. The process was carried out at the atmospheric pressure. Then, CdS buffer layers (70–100 nm in thickness) were chemically grown on the CZTS absorber layers by chemical bath deposition (CBD) after soaking the layers in deionized water (DIW) for 10 min. Subsequently, 100–400-nm thick Ga-doped ZnO window layers and comb-shaped Al collecting electrodes were fabricated by sputter deposition and electron beam deposition, respectively. Finally, the cells were separated by mechanical scribing and the Mo electrode was exposed by scratching the overlaying films.

Table 1 Progressive development of conversion efficiencies of CZTS and CZTSSe solar cells.

1988 Confirmation of photovoltaic property of CZTS Ito, K., et al. Shinshu Univ.	2010 $\eta = 6.81\%$ Wang, K., et al. IBM
1996 Confirmation of photovoltaic power of CZTS solar cells $\eta = 0.66\%$ Katagiri, H., et al. Nagaoka Nat. College of Tech. (NNCT)	2010 $\eta = 9.66\%$ CZT(S,Se) Todorov, T. K., et al. IBM
1997 Confirmation of photovoltaic power of CZTS solar cells $\eta = 2.3\%$ Friedlmeier, Th. M., et al. Stuttgart Univ.	2011 $\eta = 7.13\%$ Shin, B., et al. IBM
1999 $\eta = 2.67\%$ Katagiri, H., et al. NNCT	2011 $\eta = 7.6\%$ Eguchi, T., et al. Toyota Industries and TCRDL
2003 $\eta = 4.54\%$ Katagiri, H., et al. NNCT	2012 $\eta = 10.1\%$ CZT(S,Se) Barkhouse, D., et al. IBM
2003 $\eta = 5.45\%$ Katagiri, H., et al. NNCT	2012 $\eta = 11.1\%$ CZT(S,Se) Todorov, T. K., et al. IBM
2007 $\eta = 5.74\%$ Jimbo, K., et al. NNCT	2012 $\eta = 8.6\%$ Sugimoto, H., et al. Solar Frontier
2008 $\eta = 6.77\%$ Katagiri, H., et al. NNCT and Toyota Central R&D Labs. (TCRDL)	

3. Relationship between Composition of CZTS Thin Films and Conversion Efficiency of Solar Cells

The marked influence of the composition of the CZTS thin films on the conversion efficiency of the CZTS solar cells has been previously reported.⁽²⁰⁾ **Figures 3(a)–3(d)** show the relationships between the composition ratios and the photovoltaic properties. The Cu/(Zn + Sn) and Zn/Sn of the CZTS thin films were considered. **Figures 3(a)–3(d)** show the dependence of conversion efficiency (η), open-circuit voltage (V_{oc}), short-circuit current density (J_{sc}), and filling factor (FF), respectively, on the composition ratios of the CZTS absorber layers. The components of the

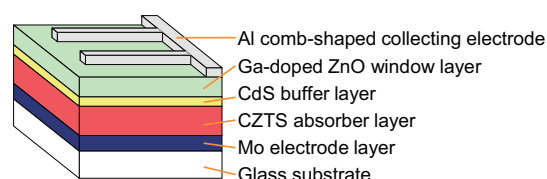


Fig. 1 Device structure of CZTS solar cells without high-resistance buffer layer and antireflection coating.

CZTS absorber layers were estimated using inductively coupled plasma-atomic emission spectroscopy (ICP-AES) and X-ray fluorescence (XRF) analysis. The current density–voltage (J – V) characteristics of the CZTS solar cells were measured

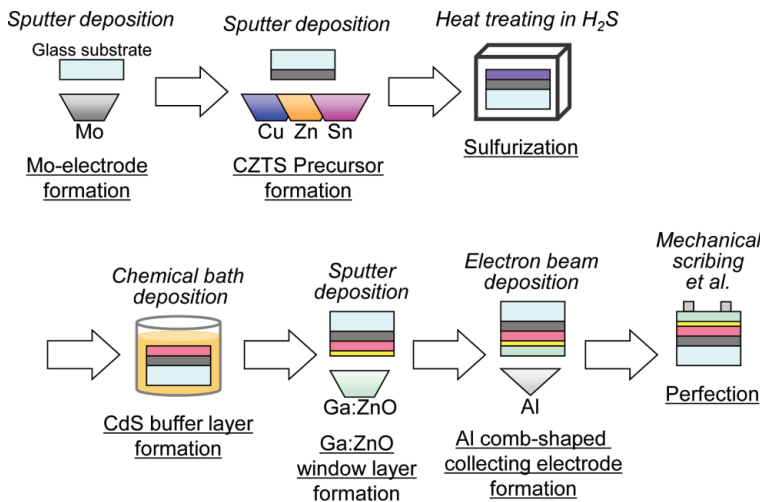


Fig. 2 Representation of conventional preparation of CZTS solar cells.

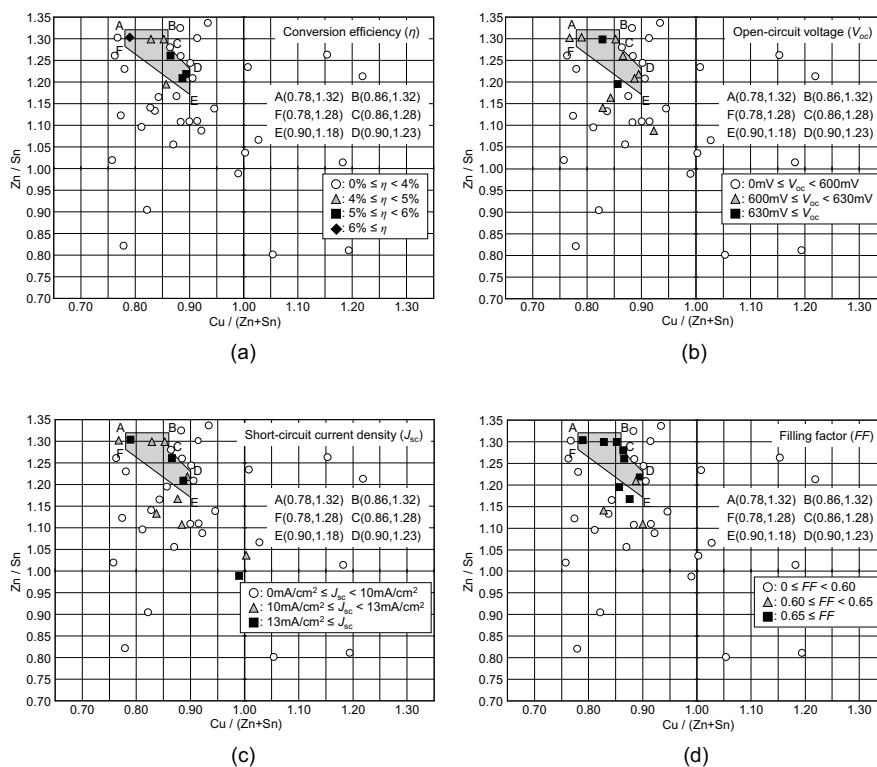


Fig. 3 Relationships between composition ratios and photovoltaic properties. Composition ratios include $\text{Cu}/(\text{Zn} + \text{Sn})$ and Zn/Sn of CZTS thin films. (a), (b), (c) and (d) show dependence of conversion efficiency (η), open-circuit voltage (V_{oc}), short-circuit current density (J_{sc}), and filling factor (FF), respectively, on composition ratio. Composition ratio ranges corresponding to high values of each photovoltaic property are located in common gray-shaded region in (a), (b), (c) and (d).

using a solar simulator under air mass (AM) 1.5 illumination (1 sun) with a power density of $100 \text{ mW}/\text{cm}^2$. The photovoltaic properties were determined from the J – V characteristics. The composition ratios corresponding to the high values of each photovoltaic property were located in a common hatched region, as shown in Figs. 3(a)–3(d). The region was narrow, indicating that precise composition control is essential to improve the conversion efficiency.

4. Crystal Structure Study

4.1 Theoretical Approach

4.1.1 Stability of Crystal Structure⁽²¹⁾

First-principle calculations for the CZTS crystal structure stability have been carried out. Calculations were performed using the plane-wave projector augmented-wave (PAW)^(22,23)

method by applying the semilocal Perdew-Burke-Ernzerhof (PBE)⁽²⁴⁾ exchange correlation functional, and the Heyd-Scuseria-Ernzerhof (HSE)⁽²⁵⁾ hybrid functional was implemented in the Vienna *ab initio* simulation package (VASP)^(26,27) code.

Here, we describe the stability of the crystal structure of CZTS. CZTS crystallizes in the kesterite structure shown in **Fig. 4(a)**. The most important structural modification is the stannite structure (**Fig. 4(b)**). The different structural modifications are related to a different order of lattice arrangement in the cation sublattice plane. The kesterite structure is characterized by alternating the cation layers of Cu–Sn, Cu–Zn, Cu–Sn, and Cu–Zn at $z = 0, 1/4, 1/2,$ and $3/4,$ respectively. The primitive cell has body centered tetragonal (BCT) crystal structure, whereas **Fig. 4(a)** shows the tetragonal supercell. In the stannite structure, the Zn–Sn layers

alternate with the Cu–Cu layers, with the primitive cell having BCT crystal structure.⁽²⁷⁾ The kesterite structure and the stannite structure belong to the space groups $\bar{I}4$ and $\bar{I}42m$, respectively. In addition to the kesterite and stannite structures, we included three structural modifications of kesterite in our study, which are shown in Figs. 4(c)–4(e). These modifications belong to the tetragonal space groups $P\bar{4}2c$, $P\bar{4}2_1m$, and $P2$, respectively. All three structures can be considered to be the modifications of the kesterite structure, where the modifications are restricted to the exchange of two ions on the cation sublattice plane (shown by green arrows in Figs. 4(c)–4(e)). In the structure shown in Fig. 4(c), the Cu and Zn atoms in the layer $z = 1/4$ are exchanged, creating a “stacking” fault with respect to the BCT kesterite structure. In the structure shown in Fig. 4(d), the Cu and Zn atoms are exchanged between the two layers to yield complete Zn and Cu layers at $z = 1/4$ and $z = 3/4$. In the final structure shown in Fig. 4(e), a Cu atom at $z = 1/2$ is exchanged with the Zn atom at $z = 3/4$. This recovers the stannite structure at the layers $z = 1/2$ and $z = 3/4$, but maintains the kesterite structure in the other two layers. Despite the nonexhaustive nature of this selection, the structural mixtures between kesterite and stannite are covered. **Table 2** summarizes the lattice parameters predicted for the five modifications shown in Fig. 4.^(28–31) In agreement with the experimental results, the kesterite structure is the most stable modification, according to both PBE and HSE, although the $P\bar{4}2c$ modification is very close in energy to the kesterite structure. This is in agreement with the experimental observations, which indicate a considerable intermixing of the Cu and Zn atoms within the Cu–Zn plane (compare (a) with (c) in Fig. 4). The stannite structure has slightly higher energy (50 meV), whereas the other two modifications, i.e., $P\bar{4}2_1m$ and $P2$, have much higher energies (200–400 meV).

4. 1. 2 Phase Stability and Defect Formation⁽³²⁾

First-principle studies of the phase stability of and defect formation in CZTS

have been carried out. The calculations were carried out using the technique mentioned previously. To accurately determine the formation energies of the defects in the dilute limit, we calculated the formation energies for different supercells, i.e., up to 512 atoms/cell, as described below. The lattice constants were fixed at the optimized values for the perfect CZTS crystal,⁽²¹⁾ while the ionic positions were relaxed until the residual forces became less than 0.2 eV/Å.

The chemical potentials μ_α were referenced to the standard elemental state, i.e., $\mu_\alpha = \mu_\alpha^0 + \Delta\mu_\alpha$, where the reference potentials μ_α^0 correspond to those of the metallic Cu, Zn, Sn, and solid state S. The allowed $\Delta\mu_\alpha$ can be determined based on the fact that CZTS must be more stable than any competing phase such as CuS, Cu₂S, SnS, SnS₂, ZnS, and Cu₂SnS₃. For a four-component system, three chemical potentials are

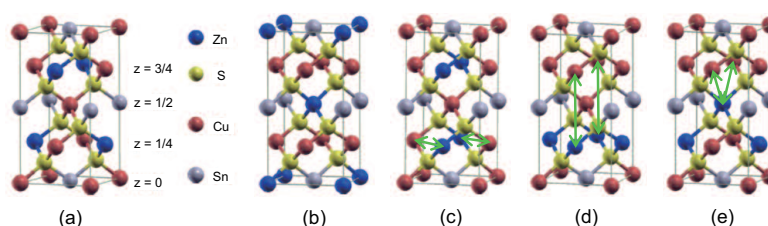


Fig. 4 Schematic representations of (a) kesterite structure ($\bar{I}4$) and (b) stannite structure ($\bar{I}42m$) emphasizing difference in metal ordering. In addition, schematic representations of three structural modifications of kesterite are shown in (c), (d) and (e), which are members of $P\bar{4}2c$, $P\bar{4}2_1m$ and $P2$ space groups, respectively. Modifications are restricted to the exchange of two ions on cation sublattice plane (shown by green arrows in (c), (d) and (e)). Atomic radii were chosen arbitrarily.

Table 2 Lattice parameters a_0 , b_0 and c_0 (in nm) of modifications of CZTS as obtained using density functional theory (PBE) and hybrid functionals (HSE) compared to experimental values. Energy difference ΔE (eV) with respect to kesterite structure and bandgap E_g (eV) is also listed.

	Experimental values	Theoretical calculation values				
		kesterite	stannite	modification		
		(a)	(b)	(c)	(d)	(e)
		$\bar{I}4$	$\bar{I}42m$	$P\bar{4}2c$	$P\bar{4}2_1m$	$P2$
a_0 (nm)	0.5427 ⁱ⁾	0.5448	0.5438	0.5446	0.5464	0.5443
b_0 (nm)						
c_0 (nm)	1.0871 ⁱ⁾	1.0889	1.0941	1.0885	1.0857	1.0892
$c_0/2a_0$	1.001	0.999	1.006	0.999	0.993	1.001
ΔE (eV)		0.0	0.054	0.012	0.390	0.272
E_g (eV)	1.44–1.51 ⁱⁱ⁾	1.487	1.295	1.458	1.206	1.073

i) Hall, S. R., et al., *Can. Mineral.*, Vol. 16 (1978), 131

ii) Seol, J. S., et al., *Sol. Energy Mater. Sol. Cells*, Vol. 75 (2003), 155
Matsushita, H., et al., *J. Cryst. Growth*, Vol. 208 (2000), 416
Scragg, J. J., et al., *Electrochem. Commum.*, Vol. 10 (2008), 63

independent and one potential is fixed by the requirement that the stoichiometrically weighted sum of the chemical potentials should be equal to the total energy of the compound, i.e., $E_p = 2\mu_{Cu} + \mu_{Zn} + \mu_{Sn} + 4\mu_S$. Using the heat of formation $\Delta H(CZTS)$ and the chemical potentials referenced to the standard elemental states $\Delta\mu_w$, the constraint can be written as $\Delta H(CZTS) = 2\Delta\mu_{Cu} + \Delta\mu_{Zn} + \Delta\mu_{Sn} + 4\Delta\mu_S$.

Two-dimensional portions of the phase stability diagram for a fixed $\Delta\mu_{Cu}$ and varying $\Delta\mu_{Zn}$ and $\Delta\mu_{Sn}$ values are shown in Fig. 5. For the Cu-rich conditions ($\Delta\mu_{Cu} = 0.0$ eV), phase boundaries between CZTS and ZnS, SnS, Cu_2SnS_3 , and CuS under Zn-rich, Sn-rich, Zn-poor, and Zn-poor and Sn-poor conditions, respectively were determined. Under Cu-rich conditions, CZTS was stable only in a very small region of the phase diagram; $\Delta\mu_{Zn}$, in particular, must be within a narrow range because CZTS competed with Cu_2SnS_3 and ZnS. The situation worsened when μ_{Cu} decreased (Cu-poor conditions). When only solid S was the competing phase, CZTS became unstable for $\Delta\mu_{Cu} < -0.41$ eV (Fig. 5(b)); on the other hand, if the formation of H_2S was allowed (e.g., if H_2 was available), the stable region was even smaller and CZTS became unstable for $\Delta\mu_{Cu} < -0.28$ eV (Fig. 5(c)). The very small phase-stability regime of CZTS has profound implications for the growth process and implies that extreme care must be taken to avoid precipitates of the six competing solid phases. As is often observed in experiments, Cu-poor and Zn-rich conditions can be used to avoid Zn-poor phases such as Cu_2SnS_3 ; however, unfortunately, to avoid the formation of ZnS precipitates, a relatively low Zn potential $\Delta\mu_{Zn} < -1.0$ eV is also required.

Next, we determined the formation energies of point defects in the charged state q , considering the vacancies of atoms at site A , $(V@A)^q$, or substitution of atom A by the atom at site B , $(B@A)^q$. Table 3 shows the defect formation energies for various types of defects. Fermi energy was fixed at the valence band maximum.

The chemical potentials at the CZTS domain boundaries were used (marked by brackets in Fig. 5). We list the results corresponding to the upper and lower bounds with and without monopole corrections; however, the results were essentially identical for both cases. The most stable defect was unambiguously Cu at Zn [$(Cu@Zn)$] with a negative formation energy for the entire allowed chemical potential range. This indicated the spontaneous formation of Cu antisite defects at high dilutions, and because Cu has a valency of 1+ and Zn has a valency of 2+, this result fully accounts for the p -type behavior usually observed in CZTS. Furthermore, Cu vacancies [$(V@Cu)$] under the Cu-poor conditions [5] and $(Zn@Sn)$ and $(Cu@Sn)$ under the Sn-poor conditions [3] also exhibited relatively low formation energies of approximately 0.2 eV. We have also calculated all the possible interstitial defects among the constituent elements. Their formation energies were >1 eV in the allowed chemical potential region. To determine the formation energy of the $(Cu@Zn)$ defect in the high-concentration region, we determined the formation energies of $(Cu@Zn)$ under

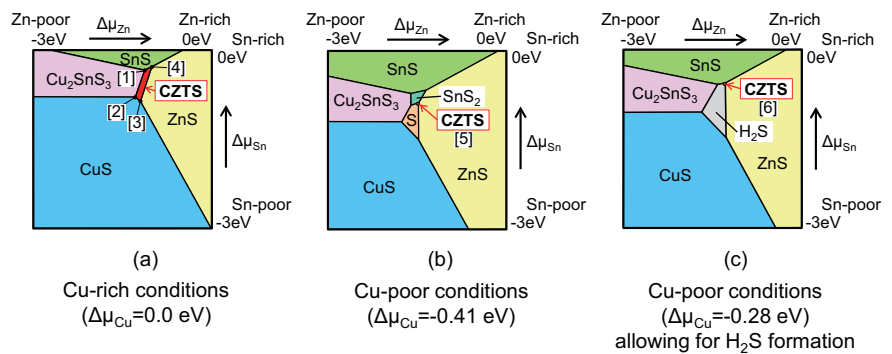


Fig. 5 Chemical potential domains allowed for CZTS phases (shown as red-shaded areas and points) in $\Delta\mu_{Zn}$ and $\Delta\mu_{Sn}$ planes for (a) Cu-rich conditions ($\Delta\mu_{Cu} = 0.0$ eV), (b) Cu-poor conditions ($\Delta\mu_{Cu} = -0.41$ eV) using solid S as the sulfur source, and (c) Cu-poor conditions ($\Delta\mu_{Cu} = -0.28$ eV) allowing for H_2S formation.

Table 3 Formation energies (in eV) of possible point defects obtained using chemical potentials at CZTS domain boundaries specified in Fig. 5. Fermi energy was fixed at the valence band maximum. Values with monopole corrections are listed in parentheses.

	(eV)					
Defects	[1]	[2]	[3]	[4]	[5]	[6]
$(Cu@Zn)$	-0.164	-0.318	-0.252	-0.064	-0.121	-0.064
$(Cu@Zn)^-$	-0.114 (0.001)	-0.268 (-0.153)	-0.202 (-0.087)	-0.015 (0.101)	-0.071 (0.044)	-0.015 (0.101)
$(Cu@Zn)^+$	0.478 (0.593)	0.632 (0.747)	0.565 (0.680)	0.378 (0.493)	0.435 (0.550)	0.378 (0.493)
$(V@Cu)$	0.590	0.590	0.590	0.590	0.182	0.315
$(V@Cu)^-$	0.591 (0.707)	0.591 (0.707)	0.591 (0.707)	0.591 (0.707)	0.183 (0.298)	0.316 (0.431)
$(Zn@Sn)$	0.599	0.291	0.158	0.532	0.419	0.532
$(Cu@Sn)$	0.698	0.236	0.170	0.732	0.562	0.732
$(V@Zn)$	0.785	0.631	0.697	0.885	0.420	0.609

the Zn-rich conditions (points [4] or [6] in Fig. 5) using fully relaxed 128-, 64-, and 16-atom supercells, without employing band filling corrections. We found a roughly linear dependence of the formation energy of a defect on the inverse volume $1/\Omega$ (where Ω is the cell volume), which became positive (endothermic) under either of the following conditions: (i) when Ω was 0.17 (nm)^3 , or (ii) when the defect concentration was $> 6 \times 10^{21} \text{ cm}^{-3}$. This indicated that the antisite defect (Cu@Zn) in CZTS is thermodynamically stable up to fairly high concentrations of defects. In practice, it would be important to control the (Cu@Zn) antisite concentration to optimize the carrier concentration in CZTS.

4.2 Experimental Approach (Thin Film)

4.2.1 Determination of Crystal Structure of Photovoltaic CZTS Thin Films⁽³³⁾

Distinguishing kesterite and stannite crystal structures by Rietveld analysis using X-ray diffraction (XRD) data is challenging because of the similarity of the two structures. Although neutron diffraction technique can more effectively distinguish between the two structures,⁽³⁴⁾ it was difficult to apply the technique to these compounds because the thin film samples were very small. Therefore, the most useful method to determine the structures was synchrotron radiation (SR)-XRD using the anomalous dispersion effect.⁽³⁵⁾ The crystal structure of the CZTS thin films fabricated by sulfurization was determined using X-ray anomalous dispersion. High static synchrotron radiation XRD data were collected from very small amounts of powder.

CZTS precursors that were $\sim 1.3 \mu\text{m}$ thick were deposited by RF magnetron co-sputtering on Mo-coated soda lime glass (SLG) substrates using three targets made of Cu (four nines), SnS (four nines), and ZnS (four nines). The pressure of the Ar sputtering gas was 0.5 Pa. The CZTS films were formed by sulfurizing the CZTS precursors at 580 °C and 540 °C for 3 h in 20 vol% H_2S balanced with N_2 . Three types of CZTS films with Cu-rich (C), stoichiometric (S), and Cu-poor (P) compositions were analyzed. Powder samples were fabricated by grinding the CZTS flakes scraped off from the CZTS films obtained on the substrates in an agate mortar. The powders were then placed in Lindemann capillaries with an inner diameter of 0.2 mm. The synchrotron XRD measurements were

carried out at BL19B2 in SPring-8. The XRD data were recorded on an imaging plate (IP) at ambient temperature. Wavelengths of 0.139–0.150 nm were used to enhance the anomalous dispersion effect close to the Cu K-edge. To prevent background emission due to the fluorescence X-rays from the samples, X-rays with wavelength longer than 0.138 nm, i.e., the absorption wavelength of the Cu K-edge spectra was used. The capillary was rotated around the longer direction to reduce the anisotropic factor. The absence of spot pattern in the Debye ring originating from the large grains in the samples was confirmed. The computer program RIETAN-FP⁽³⁶⁾ was used to simulate the XRD patterns of the two structures and to perform the Rietveld analysis.⁽³⁷⁾

We discriminated the crystal structures using the anomalous dispersion effect. We calculated the relative intensities of the 0 0 2 and 1 1 0 diffraction maxima for the kesterite and stannite structures using the atomic positions indicated in **Table 4**. The wavelength dependencies of the intensities of the 0 0 2 and 1 0 1 diffraction maxima [$I_{0\ 0\ 2}(\lambda)$, $I_{1\ 0\ 1}(\lambda)$] of the kesterite and stannite structures were simulated, as shown in **Fig. 6**. The peak intensity $I_{0\ 0\ 2}(\lambda)$ [$I_{1\ 0\ 1}(\lambda)$] of the stannite structure decreased by 30% (10%) on increasing the wavelength from 0.139 nm to 0.150 nm, while the peaks decreased by 10% (25%) for the kesterite structure. Because of the strong wavelength dependence of $I_{0\ 0\ 2}(\lambda)$ [$I_{1\ 0\ 1}(\lambda)$] for the two types of crystal structures, it was possible to distinguish the structures experimentally, despite the contamination

Table 4 Atomic positions in unit cells of kesterite and stannite structures.

Site	Atomic position for kesterite	
2a	(0, 0, 0)	(1/2, 1/2, 1/2)
2b	(0, 0, 1/2)	(1/2, 1/2, 0)
2c	(0, 1/2, 1/4)	(1/2, 0, 3/4)
2d	(0, 1/2, 3/4)	(1/2, 0, 1/4)
8g	(x, y, z)	(x+1/2, y+1/2, z+1/2)
	(x, -y, z)	(x+1/2, -y+1/2, z+1/2)
	(y, -x, -z)	(y+1/2, -x+1/2, -z+1/2)
	(-y, x, -z)	(-y+1/2, x+1/2, -z+1/2)
Site	Atomic position for stannite	
2a	(0, 0, 0)	(1/2, 1/2, 1/2)
2b	(0, 0, 1/2)	(1/2, 1/2, 0)
4d	(0, 1/2, 1/4)	(1/2, 0, 3/4)
	(0, 1/2, 3/4)	(1/2, 0, 1/4)
8g	(x, x, z)	(x+1/2, y+1/2, z+1/2)
	(-x, -x, z)	(-x+1/2, -x+1/2, z+1/2)
	(x, -x, -z)	(x+1/2, -x+1/2, -z+1/2)
	(-x, x, -z)	(-x+1/2, x+1/2, -z+1/2)

by the large grains and/or preferred orientation effects.

The $I_{002}(\lambda)$ and $I_{101}(\lambda)$ values obtained from the XRD data are shown in **Fig. 7**. $I_{002}(\lambda)$ and $I_{101}(\lambda)$ decreased monotonically with increasing wavelength along the simulated curve for the kesterite structure for all samples. This suggested that the CZTS thin films

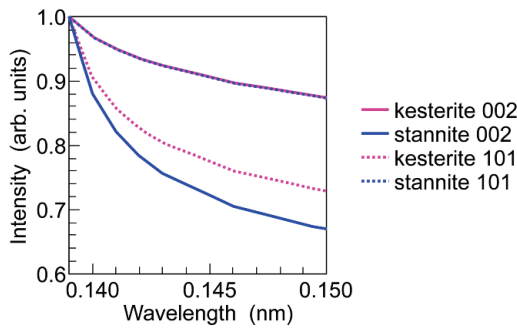


Fig. 6 Simulated wavelength dependencies of 0 0 2 and 1 0 1 diffraction peak intensities for kesterite and stannite structures. Each peak intensity was normalized to 1 1 2 main peak intensity. Although 0 0 2 peak for kesterite and 1 0 1 peak for stannite seem to show the same behavior, their intensities are slightly different. Real and imaginary components of anomalous dispersion have been reported in Ref. [34].

obtained in this experiment preferentially had kesterite structure. The Rietveld analysis was performed using the data obtained for kesterite. The refined results for a 580S sample (sulfurizing temperature: 580 °C, composition: stoichiometry) are shown in and **Table 5**. The difference pattern $I_{\text{obs}} - I_{\text{cal}}$ had a very small deviation, indicating that the variable parameters were well converged, and the reliability (R) factor was 6.02 %. As shown in Table 5, the occupancies of the 2a and 2b sites were slightly different from the stoichiometric values of the kesterite structure, while those of the 2c and 2d sites were almost stoichiometric. The composition ratio was slightly different from the stoichiometric ratio, i.e., slightly Cu-poor, Sn-poor, and Zn-rich. The atomic composition ratios were calculated as $\text{Cu}/(\text{Zn} + \text{Sn}) = 0.97$ and $\text{Zn}/\text{Sn} = 1.42$. This result had the same tendency as that reported previously on the basis of XRF analysis.^(4,20,38-41) The bond lengths from the 8g site (Sulfur site) to the 2a, 2b, 2c, and 2d sites are indicated in **Table 6**. The 2a-8g and 2d-8g lengths were ca. 8% longer than their reported values.⁽⁴²⁻⁴⁵⁾ These longer bond lengths were probably owing to the disorder of the 2a and 2d sites, which resulted in a large atomic displacement parameter B as shown in Table 5.

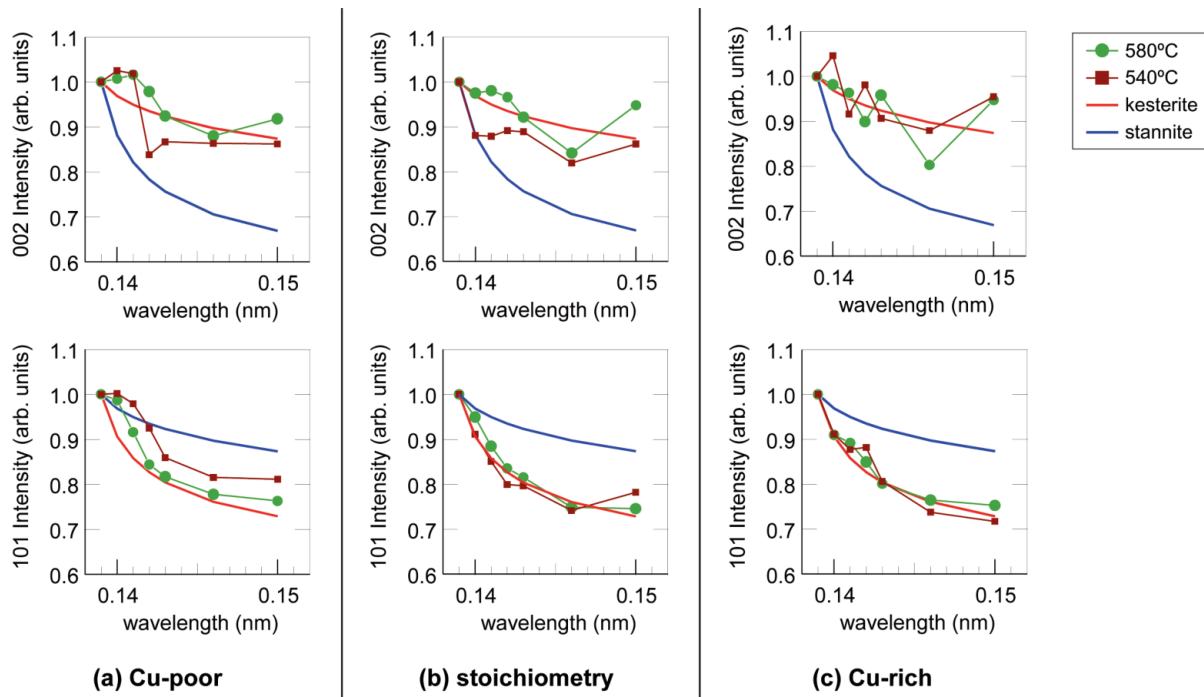


Fig. 7 Wavelength dependencies of 0 0 2 and 1 0 1 Bragg peak intensities for (a) Cu-poor, (b) stoichiometry and (c) Cu-rich CZTS thin films. Solid lines indicate simulated results. Peak intensities were normalized to that of peak at 0.139 nm.

4. 2. 2 Determination of Site Occupancies⁽⁴⁶⁾

The relationship between the composition and the kesterite structure of CZTS thin films was investigated. CZTS thin films with three different compositions were produced by sulfurization and analyzed. The Cu/(Zn + Sn) ratios of the three CZTS thin films denoted by 580C (Cu-rich composition), 580S (stoichiometric composition), and 580P (Cu-poor composition) were approximately 1.2, 1.0, and 0.8, respectively. As is well known, when $0.7 < \text{Cu}/(\text{Zn} + \text{Sn}) < 1.0$, the CZTS thin films are photovoltaic, and when $1.0 < \text{Cu}/(\text{Zn} + \text{Sn})$, the films are non-photovoltaic, as previously mentioned (Fig 3).^(2,20,40,47)

The SR-XRD measurements were carried out by the protocol described previously. The incident wavelength was 1.39 Å. RIETAN-2000⁽⁴⁸⁾ was used to perform the Rietveld analysis on the kesterite

Table 5 Crystal structure parameters obtained by Rietveld analysis of a 580S sample. Here, g , (x, y, z) and B indicate occupancy, fractional position and atomic displacement parameter, respectively.

Site	Atom	g	x	y	z	B (nm ²)
2a	Cu	0.77(5)	0	0	0	0.032(2)
	Zn	0.23				
2b	Sn	0.841(8)	0	0	1/2	0.0173(3)
	Cu	0.159				
2c	Cu	1	0	1/2	1/4	0.002
2d	Zn	0.96(4)	0	1/2	3/4	0.06(3)
	Cu	0.04				
8g	S	1	0.242(2)	0.245(2)	0.1280(4)	0.0258(5)

Space group: $\bar{1}A$, $a = 0.54380(1)$ nm, $c = 1.0857(3)$ nm.

$R_{wp} = 6.02\%$, $R_e = 3.47\%$, $S = 1.74$.

Cu : Zn : Sn : S = 3.94 : 2.38 : 1.68 : 8.0.

Table 6 Calculation and theoretical bond lengths from 8g (S) site to 2a, 2b, 2c and 2d sites. Theoretical values were obtained by summing up each atomic radius with Ref. [41].

	Sites	Bond length (nm)
Present work	2a (Cu _{0.77} Zn _{0.23})	0.2337
	2b (Sn _{0.841} Cu _{0.159})	0.2403
	2c (Cu)	0.2261
	2d (Zn _{0.96} Cu _{0.04})	0.2400
Previous work	Cu-S Ref.[42]	0.215
	Zn-S Ref.[43]	0.221
	Sn-S Ref.[44]	0.243

structure.⁽³⁷⁾ The analysis results are summarized in Fig. 8 and Tables 7(a)–7(c). There is a small difference between the experimentally obtained XRD pattern I_{obs} and the calculated XRD pattern I_{cal} obtained through the fitting process in the Rietveld analysis, as shown in Fig. 8. The difference pattern $I_{obs} - I_{cal}$ in Fig. 8 indicates that the various parameters (e.g., atomic occupancies (g) at the 2a, 2b, 2c, and 2d sites, lattice constants, position of atoms (x , y , and z), and isotropic atomic displacement parameter (B)) converge sufficiently to give the weighted profile R -factor (R_{wp}) of 5.72–6.68% and goodness of fit ($S = R_{wp}/R_e$) of 1.67–1.98. Both Cu/(Zn + Sn) and Zn/Sn composition ratios were defined as the atomic ratio of each constituent element obtained from the Rietveld analysis. The composition ratios shown in Tables 7(a)–7(c) indicate that the concentration of Sn is low while that of Zn is high. This tendency is identical to the one reported previously from XRF analyses.^(2,6,20,41,47) In this regard, we note that several reports suggest the synthesis of CZTS by the solid-state reaction of Cu₂SnS₃ and ZnS,^(32,49) because the CZTS thin films under Cu-poor and Zn-rich conditions (as in 580P) include ZnS. Therefore, multiphase Rietveld analysis of the multiphase mixtures with CZTS and ZnS was carried out. The amount of ZnS in 580P, 580C, and 580S were found to be 2.5 vol.%, 1.8 vol.%, and 1.5 vol.%, respectively. Thus, the amounts of ZnS in the CZTS thin films were negligible and contributed little to the parameters shown in Tables 7(a)–7(c).

We focused on the change of occupancies of Cu at the 2a, 2b, 2c, and 2d sites and Zn at the 2a, 2c, and 2d sites as a function of the Cu/(Zn + Sn) ratio, because

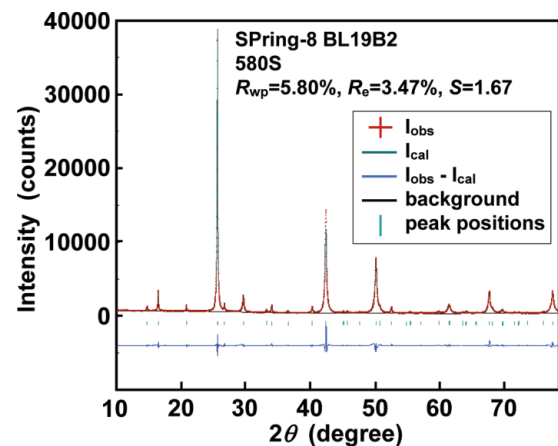


Fig. 8 Typical Rietveld analysis result (for sample 580S).

it becomes clear from Tables 7(a)–7(c) that Sn and Zn are easily substituted by Cu at the 2*b* site and 2*d* site, respectively, and Cu is easily substituted by Zn at the 2*a* and 2*c* sites. Here, we define the distributing occupancy of Cu at 2*a*, 2*b*, 2*c*, and 2*d* sites as the ratio of the occupancy of Cu at each site divided by the total amount of the occupancy of Cu at every site in Tables 7(a)–7(b). Similarly, the distributing occupancy of Zn at 2*a*, 2*c*, and 2*d* sites was calculated. **Figures 9(a)** and **9(b)** show the variation of the distributing occupancy of Cu and Zn at each site with different values of Cu/(Zn + Sn). Zn substitutes Cu at the 2*a* site with decreasing Cu/(Zn + Sn). Meanwhile, Cu substitutes Sn at the 2*b* site with increasing Cu/(Zn + Sn). The sample 580P specifically shows a marked tendency of Cu substitution of Zn at the 2*d* site

and/or Zn substitution for Cu at the 2*c* site, when compared to 580C and 580S. According to the results of calculations, as previously mentioned in 4.1.2, the antisite defect Cu at the Zn site in CZTS is thermodynamically stable up to fairly high concentrations and is the source of holes (a *p*-type semiconductor). These theoretical results support our experimental results, based on which we believe that in order to realize photovoltaic cells, it is very important that CZTS thin films have kesterite structure in which Zn at the 2*d* site is substituted by Cu and/or Cu at the 2*c* site is substituted by Zn. The amount of the substituted atoms must be very sensitive to change in the conversion efficiency of the CZTS-based thin film solar cells.

Table 7 Crystal structure parameters of (a) 580C, (b) 580S and (c) 580P samples.

(a)								
580C								
site	atom	occupancy <i>g</i>	x	y	z	B [Å ²]	composition ratio	
2 <i>a</i> -Cu	Cu	0.857 ± 0.051	0	0	0	2.91	Cu	4.36
	Zn	0.143 ± -					Zn	2.29
2 <i>b</i> -Sn	Sn	0.677 ± 0.008	0	0	1/2	1.24	Sn	1.35
	Cu	0.323 ± -					S	8.00
2 <i>c</i> -Cu	Cu	1.000 ± -	0	1/2	1/4	2.76	Cu/(Zn+Sn)	1.20
	Zn	0.000 ± -					Zn/Sn	1.69
2 <i>d</i> -Zn	Sn	- ± -	0	1/2	3/4	3.82	lattice constant [Å]	
	Zn	1.000 ± -					a	5.43957 ± 0.00015
8 <i>g</i> -S	Cu	0.000 ± -	0.272	0.233	0.126	2.45	c	10.85910 ± 0.00061
	S	1.000 ± -						
Rwp = 5.72, Rp = 4.20, RR = 10.78, Re = 3.34, S = 1.7134, d1 = 0.2524, d2 = 0.3752								
(b)								
580S								
site	atom	occupancy <i>g</i>	x	y	z	B [Å ²]	composition ratio	
2 <i>a</i> -Cu	Cu	0.639 ± 0.052	0	0	0	3.73	Cu	4.12
	Zn	0.361 ± -					Zn	2.19
2 <i>b</i> -Sn	Sn	0.842 ± 0.008	0	0	1/2	1.93	Sn	1.68
	Cu	0.158 ± -					S	8.00
2 <i>c</i> -Cu	Cu	1.000 ± -	0	1/2	1/4	3.75	Cu/(Zn+Sn)	1.06
	Zn	0.000 ± -					Zn/Sn	1.30
2 <i>d</i> -Zn	Sn	- ± -	0	1/2	3/4	1.74	lattice constant [Å]	
	Zn	0.734 ± 0.077					a	5.44115 ± 0.00014
8 <i>g</i> -S	Cu	0.266 ± -	0.272	0.233	0.126	2.64	c	10.86401 ± 0.00056
	S	1.000 ± -						
Rwp = 5.80, Rp = 4.13, RR = 9.78, Re = 3.47, S = 1.6711, d1 = 0.2826, d2 = 0.2920								
(c)								
580P								
site	atom	occupancy <i>g</i>	x	y	z	B [Å ²]	composition ratio	
2 <i>a</i> -Cu	Cu	0.615 ± 0.067	0	0	0	3.92	Cu	3.46
	Zn	0.385 ± -					Zn	2.73
2 <i>b</i> -Sn	Sn	0.902 ± 0.012	0	0	1/2	2.58	Sn	1.80
	Cu	0.098 ± -					S	8.00
2 <i>c</i> -Cu	Cu	0.498 ± -	0	1/2	1/4	3.36	Cu/(Zn+Sn)	0.76
	Zn	0.502 ± -					Zn/Sn	1.52
2 <i>d</i> -Zn	Sn	- ± -	0	1/2	3/4	3.24	lattice constant [Å]	
	Zn	0.480 ± 0.048					a	5.44239 ± 0.00006
8 <i>g</i> -S	Cu	0.520 ± -	0.272	0.233	0.126	2.65	c	10.86200 ± 0.00025
	S	1.000 ± -						
Rwp = 6.68, Rp = 4.81, RR = 11.87, Re = 3.36, S = 1.9879, d1 = 0.2889, d2 = 0.4417								

5. Formation Process of CZTS Thin Films^(17,18)

We investigated the formation processes of CZTS thin films prepared by sulfurization using H₂S. To ease the understanding of the formation of CZTS thin films from the multilayer precursors, we adopted three-layered precursors in which each layer comprised a metal or single metal-sulfide film obtained by sputter deposition.

First, we examined the reaction of the bilayers formed on Mo-coated alkali glass substrates with Cu, ZnS, Sn, and SnS as the sources. The five different bilayer systems Cu-ZnS, ZnS-Sn, ZnS-SnS, Cu-Sn, and Cu-SnS were prepared. Sulfurization was carried out by heating the bilayers to a given temperature at the heating rate of 5 °C/min and naturally cooling them to room temperature in 20 vol% H₂S balanced with N₂. The process was carried out at atmospheric pressure. The microstructures, crystal structures, and compositional properties of the sulfurized thin films were determined by scanning electron microscopy (SEM), XRD, and XRF. **Figure 10** shows the reaction processes occurring in the three bilayers (Cu-ZnS, SnS-ZnS, and Cu-SnS) on Mo layers by crystallographic study. The cross-sectional SEM

images of the three bilayers sulfurized at 200 °C or 600 °C are shown in **Fig. 11**. The ZnS layer hardly reacted with the Cu layer or the SnS layer below 600 °C. The ZnS layer contained between the Cu and the SnS layer is considered to inhibit the reaction between the two layers. Therefore, the stacked structures of the precursors with a direct contact between the Cu and the SnS(Sn) layers have the advantage of uniformly promoting the reaction.

Next, we investigated the reaction of the three-layered precursors formed on the Mo-coated substrates using Cu, Zn, ZnS, Sn, and SnS sources. The Cu-Zn-Sn, Cu-ZnS-Sn, and Cu-ZnS-SnS precursor systems were prepared. The sulfurization conditions as well as the analysis methods used were identical to those used in the bilayer systems. **Figure 12** shows the formation process of the CZTS thin films fabricated from the Cu-Zn-Sn and the Cu-ZnS-SnS three-layered precursor systems. By investigating many three-layered precursors with different stacking orders, the formation process was confirmed to be independent of the

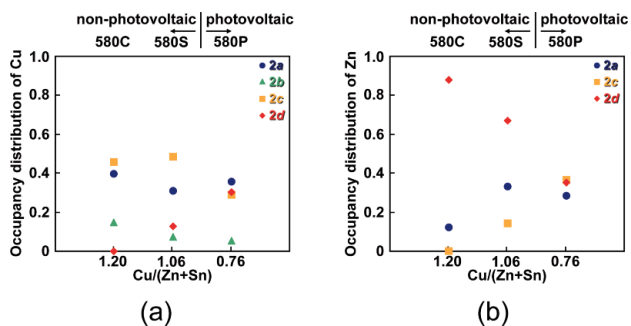


Fig. 9 Occupancy distributions of (a) Cu and (b) Zn at each site of CZTS thin films. 580P generated photovoltage while 580S and 580C did not generate photovoltage.

Precursor	Sulfurizing temperature		
	200°C	400°C	600°C
Mo/ZnS/Cu	Cu → CuS	CuS → Cu ₂ S	
Mo/ZnS/SnS		SnS → Sn ₂ S ₃	Sn ₂ S ₃ → SnS ₂
Mo/SnS/Cu	Cu → CuS	CuS + SnS → Cu ₂ SnS ₃	CuS + SnS → Cu ₂ SnS ₃ SnS → SnS ₂

Fig. 10 Reaction processes of three bilayers.

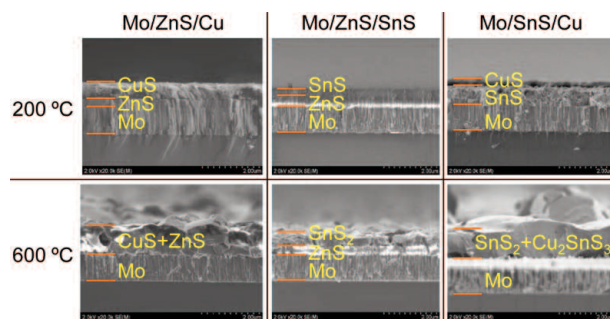


Fig. 11 Cross-sectional SEM images of three bilayers (Cu-ZnS, SnS-ZnS and Cu-SnS) sulfurized at either 200 °C or 600 °C.

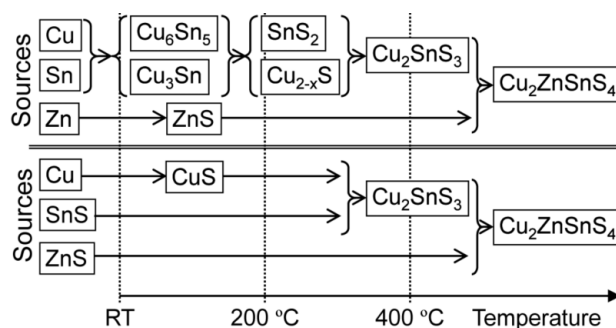
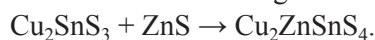


Fig. 12 Reaction processes of two-layered and three-layered systems (Cu-Sn-Zn and Cu-SnS-ZnS). CZTS thin films were necessarily formed through reaction $Cu_2SnS_3 + ZnS \rightarrow Cu_2ZnSnS_4$.

stacking structure. In our experiments, the CZTS thin films were formed through the following reaction:



We infer that the formation of a homogeneous Cu_2SnS_3 thin film and the enhancement of the reactivity of Cu_2SnS_3 and ZnS are important in the formation of homogeneous CZTS thin films. In addition, the adhesivity of the CZTS thin film on the Mo layer was high when a ZnS thin film was used as the underlayer of the precursor upon the Mo layer.

6. Preferential Etching of CZTS Thin Films⁽⁶⁾

CZTS precursors were deposited by RF magnetron co-sputtering using three targets—Cu, SnS, and ZnS on Mo-coated SLG substrates. The sulfurization process was carried out by heating the CZTS precursors to 580 °C and maintaining the temperature for 3 h in an atmosphere of 20 vol% H_2S balanced with N_2 . The CZTS absorber layers were $\sim 2.2 \mu\text{m}$ thick. The components of the CZTS absorber layers were measured using ICP-AES. The atomic ratios $\text{Cu}/(\text{Zn} + \text{Sn})$, Zn/Sn , and $\text{S}/(\text{Cu} + \text{Zn} + \text{Sn})$ were determined as ~ 0.85 , ~ 1.25 , and ~ 1.10 , respectively. The CZTS absorber layer on the Mo-coated SLG substrate (SLG/Mo/CZTS) was soaked in DIW for 10 min after fabricating the CZTS absorber layer. Then, a CdS buffer layer, a ZnO:Al window layer, and a comb-shaped Al electrode were fabricated. The J - V characteristics were measured using a solar simulator under AM 1.5 and 1 sun after soaking light for 5 min. **Figure 13** shows the J - V characteristics of the best CZTS-based solar cells with $\eta = 6.77\%$, $V_{\text{oc}} = 610 \text{ mV}$,

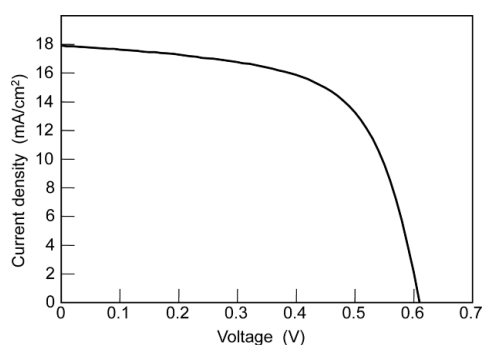


Fig. 13 J - V characteristics of the best-performing CZTS-based thin film solar cell under AM 1.5 and $100 \text{ mW}/\text{cm}^2$ illumination (of 1 sun) after light soaking for 5 min. $\eta = 6.77\%$, $V_{\text{oc}} = 610 \text{ mV}$, $J_{\text{sc}} = 17.9 \text{ mA}/\text{cm}^2$, $FF = 0.62$, $R_s = 4.25 \Omega$ and $R_{\text{sh}} = 370 \Omega$.

$J_{\text{sc}} = 17.9 \text{ mA}/\text{cm}^2$, $FF = 0.62$, series resistance (R_s) = 4.25Ω , and shunt resistance (R_{sh}) = 370Ω . The V_{oc} , J_{sc} , FF , R_s , and R_{sh} values of the CZTS solar cell with $\eta = 5.74\%$ obtained without DIW-soaking were 662 mV , $15.7 \text{ mA}/\text{cm}^2$, 0.55 , 9.04Ω , and 612Ω , respectively. It is inferred that the J_{sc} and FF of the CZTS solar cells were improved by lowering the series resistance by DIW-soaking. Therefore, to unambiguously confirm the effect of DIW-soaking, we studied the composition of the CZTS layer both before and after soaking the SLG/Mo/CZTS in DIW for 4 h. We measured the in-plane distributions of the components of the CZTS layer both before and after soaking in DIW for 4 h by electron probe X-ray micro analysis (EPMA). **Figures 14** show the in-plane distributions of oxygen in the CZTS layer both before and after soaking in DIW. Bright-point-like regions with high concentration of oxygen were scattered in the CZTS layer before soaking in DIW (Fig. 14(a)). In contrast, the concentration of oxygen in the CZTS layer fell below the measurable limit of the EPMA instrument by soaking in DIW in almost the entire sample (Fig. 14(b)). Because oxygen is probably present in the form of a metal oxide in the CZTS layer, one bright-point-like region in Fig. 14(a) is considered as one small metal oxide particle. Disappearance of the bright-point-like regions (Fig. 14(b)) showed that the metal oxide easily dissolves in water. Hence, DIW-soaking exerted a preferential etching effect on the CZTS absorber layer. Because the metal oxide apparently does not absorb light effectively, unlike CZTS, in order to improve the conversion efficiency of the solar cells it is preferable to remove the oxide from the CZTS layers by increasing the area

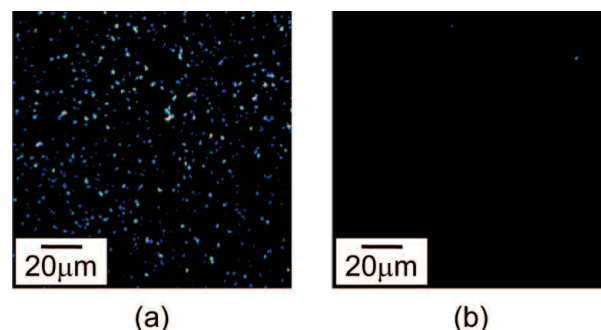


Fig. 14 In-plane distributions of oxygen in CZTS layer (a) before and (b) after soaking for 4 h in DIW measured by EPMA. Bright-point-like regions in (a) represent higher concentration areas of oxygen. In (b), bright-point-like regions are absent.

where the CdS buffer layer directly touches the CZTS absorber layer. We presumed that increasing the direct contact area between the CZTS absorber layer and the CdS buffer layer lowered the R_s of the CZTS-based solar cells.

7. Temperature Dependence of Photovoltaic Properties⁽⁵⁰⁾

We measured two solar cells with CZTS thin films fabricated under different conditions. The overall compositions of the CZTS layers were determined by ICP-AES. The J - V characteristics were measured using a solar simulator under AM 1.5 and 1 sun. The composition ratios of Cu/Zn and Cu/Sn of the CZTS layers and the photovoltaic properties of the CZTS solar cells are shown in **Table 8**. The cross-sectional microstructure and compositions of the CZTS solar cells were obtained using high angle annular dark field-scanning transmission electron microscopy (HAADF-STEM) and energy dispersive spectroscopy (EDS), respectively. Sample 1 consists of a Cu-poor and Zn-rich CZTS layer, which includes ZnS grains and large voids. Sample 2 consists of a CZTS layer with nearly stoichiometric composition, which is dense and does not contain any impurity phases. A Mo-S layer was present near the interface between the CZTS and Mo layers in each sample. Sample 2 exhibited higher J_{sc} and η compared to sample 1.

The temperature dependence of the J - V characteristics of the CZTS cells was determined using the physical properties measurement system (PPMS) (Quantum Design). The sample was placed in the helium-filled sample holder. A halogen lamp (SCHOTT, Mega Light 100) with output wavelength in the range 400–900 nm was used as the light source. The surface of the CZTS solar cell was exposed to the light through an optical fiber bundle. The light intensity was ~ 10 mW/cm², which was approximately 10% of 1 sun. **Figure 15** shows the J - V curves of sample 1 at various temperatures under illumination.

Table 8 Compositional and photovoltaic properties of sample 1 and sample 2.

	Composition		Impurity	Photovoltaic properties			
	Cu/Zn	Cu/Sn		η (%)	J_{sc} (mA/cm ²)	V_{oc} (V)	FF
sample 1	1.50	1.80	ZnS	4.5	12.0	0.61	0.62
sample 2	1.85	1.95	None	6.8	18.5	0.59	0.62

The shapes of the J - V curves indicate higher FF s in the range 200–300 K. The V_{oc} increases with decreasing temperature. The V_{oc} at 200 and 100 K were 0.85 and 1.0 V, respectively. These values were higher than the V_{oc} (~ 0.6 V) at room temperature. The J - V curves of sample 2 showed a temperature dependence similar to that of sample 1, regardless of the difference in the composition and microstructure of the CZTS layers. **Figure 16** shows the relationship between the temperature and V_{oc} for both the CZTS solar cells. Several models of electric mechanisms in heterojunction semiconductor devices have been suggested, and Rau et al. proposed the electric loss mechanisms in heterojunction solar cells.^(51,52) J and V_{oc} were expressed as $J = J_{00} \cdot \exp\{(qV - E_a)/(n \cdot k_B \cdot T)\}$ and $V_{oc} = E_a/q - \{n \cdot k_B \cdot (T/q)\} \cdot \ln(J_{00}/J_L)$, where E_a is the activation energy of dominant recombination, n is the diode ideality factor, J_{00} is the reverse saturation current prefactor, J_L is photocurrent, k_B is the Boltzmann constant, T is temperature, and q is the elementary charge. The V_{oc} s of both the samples increased linearly with decreasing temperature in the range 150–350 K. The V_{oc} at 0 K on each extrapolation

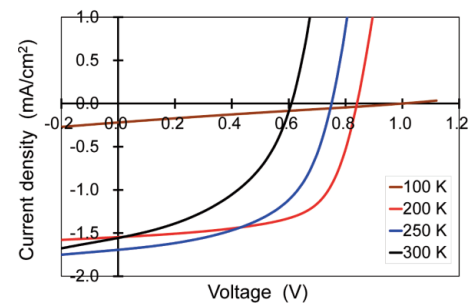


Fig. 15 Temperature dependence of J - V curves of CZTS cells (sample 1) under illumination.

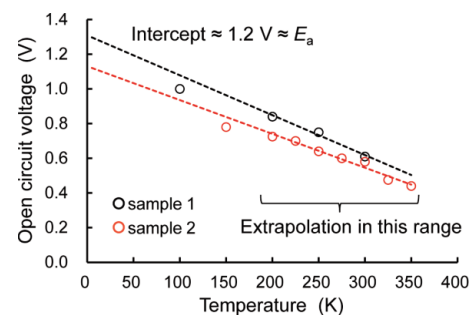


Fig. 16 Relationships between temperature and open circuit voltage in CZTS cells (sample 1 and sample 2).

plot of V_{oc} vs. T (in Fig. 16) was approximately 1.2 V, which is E_a/q according to the second equation. The difference in E_a between the two CZTS thin films was ~ 0.1 eV. In the case of the high-performance CIGS solar cells, the E_a was nearly equal to the bandgap energy (E_g) of CIGS, and thus, the V_{oc} at room temperature was improved.^(41,42) In the case of CZTS solar cells, $E_a/q = \sim 1.2$ V, which was significantly lower than the value estimated by the E_g of CZTS (1.4–1.5 eV). This suggests that the low V_{oc} of the CZTS solar cells was probably caused by carrier recombination at the interface between the CZTS and CdS layers. Improving the interface can be one of the key points to realize the high-performance CZTS solar cells.

8. High-performance CZTS Solar Cells^(17,18)

Three-layered CZTS precursors, 700–800 nm in thickness, were deposited by RF magnetron sputtering using Cu, Sn, and ZnS as the targets on Mo-coated alkali-glassa substrates. The (alkali glass/Mo)/ZnS/Sn/Cu/ precursor structure was adopted to fabricate the solar cells. Sulfurization was carried out by heating the precursors to 580 °C and maintaining the samples at this temperature for 30 min in 20 vol% H₂S balanced with N₂ at the atmospheric pressure. The heating and cooling rates were 5 and -5 °C/min, respectively. The atomic ratios Cu/(Zn + Sn), Cu/Sn, and Zn/Sn were estimated as

0.80–0.90, 1.65–1.85, and 1.02–1.10 by XRF analysis, respectively. Analysis by XRD confirmed the crystal structure to be that of kesterite. The cell structure did not include a high-resistance buffer layer and an antireflection coating. CdS buffer layers (70–100 nm thick), Ga-doped ZnO window layers of ~ 100 nm in thickness, and comb-shaped Al electrodes were fabricated.

The cross-sectional scanning transmission electron microscopy (STEM) bright field image of the solar cell is shown in Fig. 17. The CZTS absorber layer comprised densely packed large grains with low surface roughness. The grain size was larger in the three-layered precursors than in the four-layered ones. Figure 18 presents the current (I) – voltage (V) characteristics of the best-performing CZTS solar cells

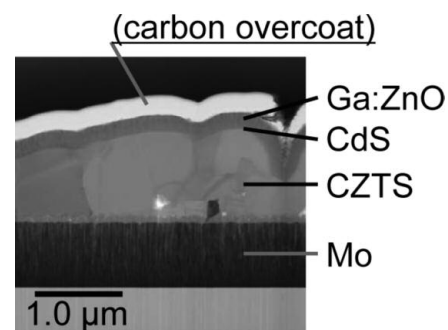


Fig. 17 Cross-sectional STEM bright-field image of CZTS solar cell.

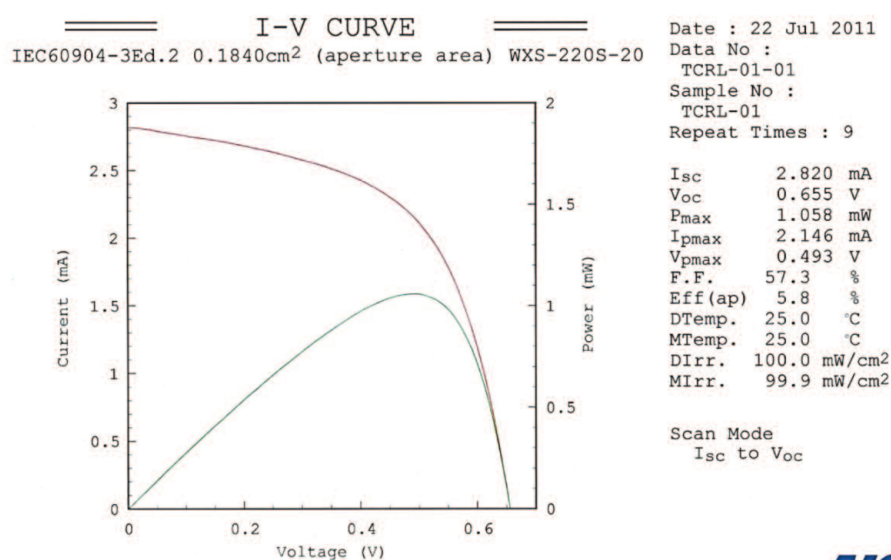


Fig. 18 I – V characteristics of the best-performing CZTS solar cell measured at AIST.

measured at the National Institute of Advanced Industrial Science and Technology (AIST), Japan. The I - V characteristics of the solar cells were measured using a solar simulator under AM 1.5 and 1 sun. The values of η in the aperture area (0.184 cm^2), V_{oc} , J_{sc} in the aperture area, and FF were 5.8%, 655 mV, 15.33 mA/cm^2 , and 57.3%, respectively. Because the active area of the best-performing CZTS solar cell was 0.140 cm^2 , η and J_{sc} in the active area were 7.6% and 20.14 mA/cm^2 , respectively. **Figure 19** shows the external quantum efficiency (EQE) spectrum of the best-performing CZTS solar cell. The EQE peak was higher than 80% in the spectral region ranging from 540 to 640 nm. The decline of the EQE in the 400–540 nm wavelength range was caused by the optical absorption of the CdS buffer layer. The EQE was lower than 80% in the 640–800 nm wavelength range. The image of an electron beam induced current (EBIC) signal on the SEM image of the CZTS solar cell is shown in **Fig. 20**. The EBIC signal presented a patchy pattern on the CZTS absorber layer around the interface between the CZTS absorber and CdS buffer layers. Though the uniformity of the power generation

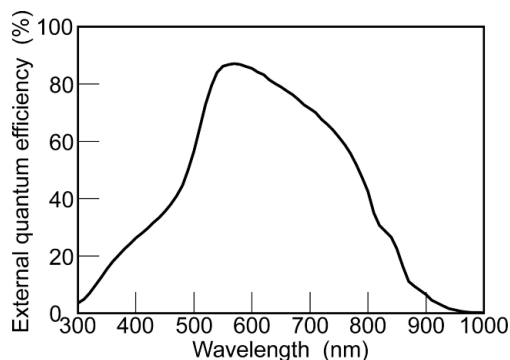


Fig. 19 EQE spectrum of the best-performing CZTS solar cell.

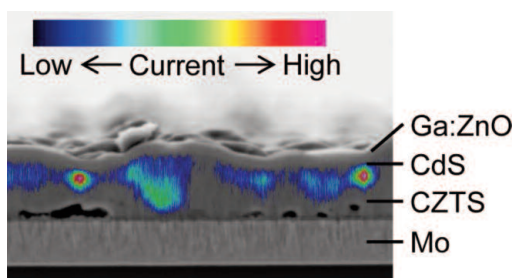


Fig. 20 Image of EBIC signal on cross-sectional SEM image of the best-performing CZTS solar cell.

region was still poor, the conversion efficiency reached 7.6%. We believe the conversion efficiency will substantially improve with power generation at the whole region.

9. Conclusions

We have described the outcomes of several researches and developments that have taken place in the fabrication of CZTS thin films and CZTS solar cells in which we have been closely involved. In the section on the crystallographic study of CZTS thin films, we described the fundamental crystallographic properties obtained by theoretical researches using first-principle calculations such as the plane-wave projector augmented-wave method and experimental studies that use synchrotron radiation XRD. The theoretical studies showed that Cu substitution at the Zn site is the most stable defect and acts as the dominant acceptor in CZTS. The experimental studies showed that the CZTS thin films that constitute the high-performing solar cells possess the kesterite crystal structure, with the Zn at the $2d$ site substituted by Cu and/or with Cu at the $2c$ site substituted by Zn. In addition, the fabrication of the CZTS thin films by sulfurization was found to necessarily take place through the reaction $\text{Cu}_2\text{SnS}_3 + \text{ZnS} \rightarrow \text{Cu}_2\text{ZnSnS}_4$. We succeeded in improving the conversion efficiency of the CZTS thin film solar cells by analyzing the sulfurization conditions. The conversion efficiency of the best-performing CZTS solar cell was 7.6%. The lower efficiencies of the CZTS solar cells compared to that of the CIGS solar cells could be attributed to the presence of an enormous number of recombination centers between the CZTS absorber and CdS buffer layers.

Acknowledgements

We sincerely appreciate Prof. H. Katagiri, K. Jimbo, and Dr. T. Washio, Nagaoka National College of Technology, Japan, for collaborating in the study of the CZTS solar cells. We thank Prof. D. Kresse, Universität Wien, Austria, for supporting our investigations by performing first-principle calculations. We also thank Dr. M. Sato and Dr. T. Koganezawa, the Japan Synchrotron Radiation Research Institute, Japan, for carrying out the (SR)-XRD measurements. We are grateful to T.

Eguchi and T. Maki, Toyota Industries Co., Japan, for their support in the investigation of the CZTS solar cells. We thank Dr. Y. Hishikawa, National Institute of Advanced Industrial Science and Technology, Japan, for measuring the $I-V$ characteristics. We appreciate Dr. T. Motohiro, Dr. K. Higuchi, and Dr. T. Ikuno, Toyota Central R&D Labs. Inc., Japan, for taking part in fruitful and profound discussions and for their kind encouragement.

References

- (1) Katagiri, H., "Cu₂ZnSnS₄ Thin Film Solar Cells", *Thin Solid Films*, Vol. 480-481 (2005), pp. 426-432.
- (2) Jimbo, K., Kimura, R., Kamimura, T., Yamada, S., Maw, W. S., Araki, H., Oishi, K. and Katagiri, H., "Cu₂ZnSnS₄-type Thin Film Solar Cells Using Abundant Materials", *Thin Solid Films*, Vol. 515, No. 15 (2007), pp. 5997-5999.
- (3) Ito, K. and Nakazawa, T., "Atom-Beam Sputtered Indium-Tin Oxide-Films", *Jpn. J. Appl. Phys. Part 1*, Vol. 27, No. 11 (1988), pp. 2094-2097.
- (4) Katagiri, H., Sasaguchi, N., Hando, S., Hoshiono, S., Ohashi, J. and Yokota, T., "Preparation and Evaluation of Cu₂ZnSnS₄ Thin Films by Sulfurization of EB Evaporated Precursors", *Sol. Energy Mater. Sol. Cells*, Vol. 49, No. 1-4 (1997), pp. 407-414.
- (5) Friedlmeier, Th. M., Wieser, N., Walter, T., Dittrich, H. and Schock, H. W., *14th European PVSEC*, (1997), P4B. 10.
- (6) Katagiri, H., Jimbo, K., Yamada, S., Kamimura, T., Maw, W. S., Fukano, T., Ito, T. and Motohiro, T., "Enhanced Conversion Efficiencies of Cu₂ZnSnS₄-Based Thin Film Solar Cells by Using Preferential Etching Technique", *Appl. Phys. Express*, Vol. 1, No. 4 (2008), 041201.
- (7) Barkhouse, D. A. R., Gunawan, O., Gokmen, T., Todorov, T. K. and Mitzi, D. B., "Device Characteristics of a 10.1% Hydrazine-Processed Cu₂ZnSn(S₂S)₄ Solar Cell", *Prog. Photovolt: Res. Appl.*, Vol. 20, No. 1 (2012), pp. 6-11.
- (8) Todorov, T. K., Tang, J., Bag, S., Gunawan, O., Gokmen, T., Zhu, Y. and Mitzi, D. B., "Beyond 11% Efficiency: Characteristics of State-of-the-Art Cu₂ZnSn(S,Se)₄ Solar Cells", *Adv. Energy Mater.*, Vol. 3, No. 1 (2013), pp. 34-38.
- (9) Wang, K., Gunawan, O., Todorov, T., Shin, B., Chey, S. J., Bojarczuk, N. A., Mitzi, D. and Guha, S., "Thermally Evaporated Cu₂ZnSnS₄ Solar Cells", *Appl. Phys. Lett.*, Vol. 97, (2010), 143508.
- (10) Sugimoto, H., Hiroi, H., Sakai, N., Muraoka, S. and Katou, T., "Over 8% Efficiency Cu₂ZnSnS₄ Submodules with Ultra-Thin Absorber", *Proc. of the 38th IEEE Photovoltaic Specialists Conf.*, (2012), pp. 2997-3000.
- (11) Cao, Y. Y., Denny, M. S., Casper, J. V., Farneth, W. E., Gio, Q. J., Ionkin, A. S., Johnson, L. K., Lu, M. J., Malajovich, I., Radu, D., Rosenfeld, H. D., Choudhury, K. R. and Wu, W., "High-Efficiency Solution-Processed Cu₂ZnSn(S,Se)₄ Thin-Film Solar Cells Prepared from Binary and Ternary Nanoparticles", *J. Am. Chem. Soc.*, Vol. 134, No. 38 (2012), pp. 15644-15647.
- (12) Shin, B., Zhu, Y., Bojarczuk, N. A., Chey, S. J. and Guha, S., "Control of an Interfacial MoSe₂ Layer in Cu₂ZnSnSe₄ Thin Film Solar Cells: 8.9% Power Conversion with a TiN Diffusion Barrier", *Appl. Phys. Lett.*, Vol. 101, No. 5 (2012), 053903.
- (13) Katagiri, H., et al., *Tech. Digest of PVSEC-9*, (1996), p. 745.
- (14) Katagiri, H., Jimbo, K., Moriya, K. and Tsuchida, K., "Solar Cell without Environmental Pollution by Using CZTS Thin Film", *Proc. of 3rd World Conf. of Photovoltaic Energy conversion*, Vols. A-C (2003), pp. 2874-2879.
- (15) Katagiri, H., "Cu₂ZnSnS₄ Thin Film Solar Cells", *Thin Solid Films*, Vol. 480 (2004), pp. 426-432.
- (16) Todorov, T. K., Reuter, K. B. and Mitzi, D. B., "High-Efficiency Solar Cell with Earth-Abundant Liquid-Processed Absorber", *Adv. Mater.*, Vol. 22, No. 20 (2010), p. E156-E159.
- (17) Eguchi, T., Maki, T., Tajima, S., Ito, T. and Fukano, T., "Cu₂ZnSnS₄ Solar Cell with 7.6% Efficiency", *Tech. Digest of PVSEC-21*, (2011), p. 4D-3P-24.
- (18) Fukano, T., Tajima, S. and Ito, T., "Enhancement of Conversion Efficiency of Cu₂ZnSnS₄ Thin Film Solar Cells by Improvement of Sulfurization Conditions", *Appl. Phys. Express*, Vol. 6, No. 6 (2013), p.062301.
- (19) Katou, T., et al., *Prog. of 27th EU-PVSEC*, (2012)
- (20) Fukano, T., Motohiro, T. and Katagiri, H., Unexamined Patent Pub. 2010-215497 (in Japanese).
- (21) Paier, J., Asahi, R., Nagoya, A. and Kresse, G., "Cu₂ZnSnS₄ as a Potential Photovoltaic Material: A Hybrid Hartree-fock density Functional Theory Study", *Phys. Rev. B*, Vol. 79, No. 11 (2009), 115126.
- (22) Blöchl, P. E., "Projector Augmented-Wave Method", *Phys. Rev. B*, Vol. 50, No. 24 (1994), pp. 17983-17979.
- (23) Kresse, G. and Joubert, D., "From Ultrasoft Pseudopotentials to Projector Augmented-wave Method", *Phys. Rev. B*, Vol. 59, No. 3 (1999), pp. 1758-1775.
- (24) Perdew, J. P., Burke, K. and Ernzerhof, M., "Generalized Gradient Approximation Made Simple", *Phys. Rev. Lett.*, Vol. 77, No. 18 (1996), pp. 3865-3868.
- (25) Heyd, J., Scuseria, G. E. and Ernzerhof, M., "Hybrid Functionals Based on a Screened Coulomb Potential", *J. Chem. Phys.*, Vol. 116, No. 18 (2003), pp. 8207-8215.
- (26) Kresse, G. and Furthmüller, J., "Efficiency of Ab-initio Total Energy Calculations for Metals and Semiconductors Using a Plane-wave Basis Set", *Comput. Mater. Sci.*, Vol. 6, No. 1 (1996), pp. 15-50.
- (27) Kresse, G. and Furthmüller, J., "Efficient Iterative Schemes for Ab Initio Total-energy Calculations

- Using a Plane-wave basis Set”, *Phys. Rev. B*, Vol. 54, No. 16 (1996), pp. 11169-11186.
- (28) Hall, S. R., Szymanski, J. T. and Stewart, J. M., “Kesterite, $\text{Cu}_2(\text{Zn,Fe})\text{SnS}_4$ and Stannite, $\text{Cu}_2(\text{Fe,Zn})\text{S}_4$, Structurally Similar but Distinct Minerals”, *Can. Mineral.*, Vol. 16, No. 2 (1978), pp. 131-137.
- (29) Seol, J. S., Lee, S. Y., Lee, J. C., Nam, H. D. and Kim, K. H., “Electrical and Optical Properties of $\text{Cu}_2\text{ZnSnS}_4$ Thin Films Prepared by RF Magnetron Sputtering Process”, *Sol. Energy Mater. Sol. Cells*, Vol. 75, No. 1-2 (2003), pp. 155-162.
- (30) Matsushita, H., Maeda, T., Katsui, A. and Takizawa, T., “Thermal Analysis and Synthesis from the Melts of Cu-based Quaternary Compounds Cu-III-IV-VI and Cu_2 -II-IV-VI₄ (II = Zn, Cd; III = Ga, In; IV = Ge, Sn; VI = Se)”, *J. Cryst. Growth*, Vol. 208, No. 1-4 (2000), pp. 416-422.
- (31) Scragg, J. J., Dale, P. J. and Peter, L. M., “Towards Sustainable Materials for Solar Energy Conversion: Preparation and Photoelectrochemical Characterization of $\text{Cu}_2\text{ZnSnS}_4$ ”, *Electrochem. Commun.*, Vol. 10, No. 4 (2008), pp. 639-642.
- (32) Nagoya, A., Asahi, R., Wahn, R. and Kresse, G., “Defect Formation and Phase Stability of $\text{Cu}_2\text{ZnSnS}_4$ Photovoltaic Material”, *Phys. Rev. B*, Vol. 81, No. 11 (2010), 113202.
- (33) Nozaki, H., Fukano, T., Ohta, S., Seno, Y., Katagiri, H. and Jimbo, K., “Crystal Structure Determination of Solar Cell Materials: $\text{Cu}_2\text{ZnSnS}_4$ Thin Films Using X-ray Anomalous Dispersion”, *J. Alloys Comp.*, Vol. 524 (2012), pp. 22-25.
- (34) Schorr, S., Hoebler, H. -J. and Tovar, M., “A Neutron Diffraction Study of the Stannite-Kesterite Solid Solution Series”, *Eur. J. Mineral.*, Vol. 19, No. 1 (2007), pp. 65-73.
- (35) Kissel, L. and Pratt, R. H., “Corrections to Tabulated Anomalous-Scattering Factors”, *Acta Crystallogr. A*, Vol. 46 (1990), pp. 170-175.
- (36) Izumi, F. and Momma, K., “Three-dimensional Visualization in Powder Diffraction”, *Solid State Phenom.*, Vol. 130 (2007), pp. 15-20.
- (37) Rietveld, H. M., “A Profile Refinement Method for Nuclear and Magnetic Structure”, *J. Appl. Cryst.*, Vol. 2 (1969), pp. 65-71.
- (38) Oishi, K., Saito, G., Ebina, K., Nagahashi, M., Jimbo, K., Maw, W. S., Katagiri, H., Yamazaki, M., Araki, H. and Takeuchi, A., “Growth of $\text{Cu}_2\text{ZnSnS}_4$ Thin Films on Si (100) Substrates by Multisource Evaporation”, *Thin Solid Films*, Vol. 517, No. 4 (2008), pp. 1449-1452.
- (39) Araki, H., Mikaduki, A., Kubo, Y., Sato, T., Jimbo, K., Maw, W. S., Katagiri, H., Yamazaki, M., Oishi, K. and Takeuchi, A., “Preparation of $\text{Cu}_2\text{ZnSnS}_4$ Thin Films by Sulfurization of Stacked Metallic Layers”, *Thin Solid Films*, Vol. 517, No. 4 (2008), pp. 1457-1460.
- (40) Araki, H., Kubo, Y., Mikaduki, A., Jimbo, K., Maw, W. S., Katagiri, H., Yamazaki, M., Oishi, K. and Takeuchi, A., “Preparation of $\text{Cu}_2\text{ZnSnS}_4$ Thin Films by Sulfurizing Electroplated Precursors”, *Sol. Energy Mater. Sol. Cells*, Vol. 93, No. 6-7 (2009), pp. 996-999.
- (41) Katagiri, H., Jimbo, K., Maw, W. S., Oishi, K., Yamazaki, M., Araki, H. and Takeuchi, A., “Development of CZTS-Based Thin Film Solar Cells”, *Thin Solid Films*, Vol. 517 No. 7 (2009), pp. 2455-2460.
- (42) Pyykko, P. and Atsumi, M., “Molecular Single-bond Covalent Radii for Elements 1-118”, *Chem.-A Euro. J.*, Vol. 15, No. 1 (2009), pp. 186-197.
- (43) Fjellvåg, H., Grønvold, F., Stølen, S., Andresen, A. F., Müller-Käfer, R. and Simon, A., “Low-temperature Structural Distortion in CuS ”, *Z. Kristallogr.*, Vol. 184, No. 1-2 (1988), pp. 111-121.
- (44) Yeh, C.-Y., Lu, Z. W., Froyen, S. and Zunger, A., “Zinc-Blende-Wurtzite Polytypism in Semiconductors”, *Phys. Rev. B*, Vol. 46, No. 16 (1992), pp. 10086-10097.
- (45) Wyckoff, R. W. G., *Crystal Structures*, vol. 85, second edition (1963), Interscience Publishers.
- (46) Washio, T., Nozaki, H., Fukano, T., Motohiro, T., Jimbo, K. and Katagiri, H., “Analysis of Lattice Site Occupancy in Kesterite Structure of $\text{Cu}_2\text{ZnSnS}_4$ Films Using Synchrotron Radiation X-ray Diffraction”, *J. Appl. Phys.*, Vol. 110, No. 7 (2011), 074511.
- (47) Katagiri, H., Jimbo, K., Tahara, M., Araki, H. and Oishi, K., “The Influence of the Composition Ratio on CZTS-based Thin Film Solar Cells”, *Proc. of Symposium on Thin-Film Compound Semiconductor Photovoltaics*, Vol. 1165 (2010), pp. 125-136, MRS.
- (48) Izumi, F. and Ikeda, T., “A Rietveld-analysis Program RIETAN-98 and Applications to Zeolites”, *Mater. Sci. Forum*, Vol. 321-324 (2000), pp. 198-205.
- (49) Schurr, R., Hölzing, A., Jost, S., Hock, R., Voß, T., Schulze, J., Kirbs, A., Ennaoui, A., Lux-Steiner, M., Weber, A., Kötschau, I. and Schock, H. -W., “The Crystallisation of $\text{Cu}_2\text{ZnSnS}_4$ Thin Film Solar Cell Absorbers from Co-electroplated Cu-Zn-Sn Precursors”, *Thin Solid Films*, Vol. 517, No. 7 (2009), pp. 2465-2468.
- (50) Tajima, S., Katagiri, H., Jimbo, K., Sugimoto, N. and Fukano, T., “Temperature Dependence of $\text{Cu}_2\text{ZnSnS}_4$ Photovoltaic Cell Properties”, *Appl. Phys. Express*, Vol. 5, No. 8 (2012), 082302.
- (51) Rau, U., Jasenek, A., Schock, H. W., Engelhardt, F. and Meyer, Th., “Electronic Loss Mechanisms in Chalcopyrite Based Heterojunction Solar Cells”, *Thin Solid Films*, Vol. 361-362 (2000), pp. 298-302.
- (52) Rau, U., “Tunneling-Enhanced Recombination in $\text{Cu}(\text{In,Ga})\text{Se}_2$ Heterojunction Solar Cells”, *Appl. Phys. Lett.*, Vol. 74, No. 1 (1999), pp. 111-113.

Fig. 4 and Table 2

Reprinted from Phys. Rev. B, Vol. 79 (2009), 115126, Paier, J., Asahi, R., Nagoya, A. and Kresse G., Cu₂ZnSnS₄ as a Potential Photovoltaic Material: A Hybrid Hartree-Fock Density Functional Theory Study, © 2009 APS, with permission from American Physical Society.

Fig. 5 and Table 3

Reprinted from Phys. Rev. B, Vol. 81 (2010), 113202, Nagoya, A., Asahi, R., Wahn, R. and Kresse, G., Defect Formation and Phase Stability of Cu₂ZnSnS₄ Photovoltaic Material, © 2010 APS, with permission from American Physical Society.

Fig. 6, Tables 4-6 and Section 4.2.1

Reprinted from J. Alloys Comp., Vol. 524 (2012), pp. 22-25, Nozaki, H., Fukano, T., Ohta, S., Seno, Y., Katagiri, H. and Jimbo, K., Crystal Structure Determination of Solar Cell Materials: Cu₂ZnSnS₄ Thin Films Using X-ray Anomalous Dispersion, © 2012 Elsevier, with permission from Elsevier.

Figs. 8-9 and Table 7

Reprinted from J. Appl. Phys., Vol. 110, No. 7 (2011), 074511, Washio, T., Nozaki, H., Fukano, T., Motohiro, T., Jimbo, K. and Katagiri, H., Analysis of Lattice Site Occupancy in Kesterite Structure of Cu₂ZnSnS₄ Films Using Synchrotron Radiation X-ray Diffraction, © 2011 AIP, with permission from American Institute of Physics.

Figs. 13-14

Reprinted from Appl. Phys. Express, Vol. 1, No. 4 (2008), 041201, Katagiri, H., Jimbo, K., Yamada, S., Kamimura, T., Maw, W. S., Fukano, T., Ito, T. and Motohiro, T., Enhanced Conversion Efficiencies of Cu₂ZnSnS₄-based Thin Film Solar Cells by Using Preferential Etching Technique, © 2008 JSAP, with permission from the Japan Society of Applied Physics.

Figs. 15-16 and Table 8

Reprinted from Appl. Phys. Express, Vol. 5, No. 8 (2012), 082302, Tajima, S., Katagiri, H., Jimbo, K., Sugimoto, N. and Fukano, T., Temperature Dependence of Cu₂ZnSnS₄ Photovoltaic Cell Properties, © 2012 JSAP, with permission from the Japan Society of Applied Physics.

Figs. 17 and 19-20

Reprinted from Appl. Phys. Express, Vol. 6, No. 6 (2013), 062301, Fukano, T., Tajima, S. and Ito, T., Enhancement of Conversion Efficiency of Cu₂ZnSnS₄ Thin Film Solar Cells by Improvement of Sulfurization Conditions, © 2013 JSAP, with permission from the Japan Society of Applied Physics.

Tatsuo Fukano

Research Field:

- Development of Functional Thin Films for Solar Cells and Electronic Devices

Academic Degree: Dr.Eng.

Academic Societies:

- The Japan Society of Applied Physics
- The Physical Society of Japan

Awards:

- R&D 100 Award, Research & Development Magazine, 2000
- Best Poster Award, Organization Committee of EXPO World Conference on Wind Energy, Renewable Energy, Fuel Cell and Exhibition, 2005



Hiroshi Nozaki

Research Fields:

- Crystal Structure and Ion-conduction Analysis Using X-ray
- Neutron and μ SR.

Academic Degree: Dr.Eng.

Academic Societies:

- The Physical Society of Japan
- The Japan Institute of Metals
- The Japanese Society for Synchrotron Radiation Research
- The Japanese Society for Neutron Science
- Society of Muon and Meson Science of Japan



Shin Tajima

Research Field:

- Magnetic Materials and Photovoltaic Materials

Academic Degree: Dr.Eng.

Academic Societies:

- The Japan Society of Applied Physics
- The Magnetic Society of Japan
- The Ceramic Society of Japan
- Japan Society of Powder and Powder Metallurgy

Award:

- Japan Society of Powder and Powder Metallurgy Paper Award, 2005



Tadayoshi Ito

Research Field:

- Development of Thin Films for Solar Cells and Photocatalysts

Academic Societies:

- Corporate Environmental Achievement Award, the American Ceramic Society, 2006
- Ceramic Prize, the Ceramic Society of Japan, 2008



Akihiro Nagoya

Research Field:

- First Principles Calculations

Academic Society:

- The Physical Society of Japan



Ryoji Asahi

Research Fields:

- Computational Materials Design for Development of Functional Materials such as Thermoelectrics Photocatalysts, and Photovoltaics

Academic Degree: Ph.D.

Academic Societies:

- The Japan Society of Applied Physics
- American Physical Society
- The Japan Institute of Metals

Awards:

- Advanced Technology Award, the Japan Fine Ceramics Association, 2003
- Corporate Environmental Achievement Award, the American Ceramic Society, 2006
- Technical Development Award, the Chemical Society of Japan, 2006
- The Best Poster Award, International Conf. on Thermoelectrics, 2013

